PAPER

Check for updates

Corrosion kinetics of pure metals (Fe, Cr, Ni) and alloys (A709, SS316) in thermal and chemical purified molten chloride salt

Mingyang Zhang, [iD] Amanda Leong, [iD] Siheng Ren and Jinsuo Zhang*

There has been notable research interest in utilizing chloride molten salt as both a heat transfer and thermal energy storage medium in nuclear and solar energy systems. However, a significant concern remains regarding the compatibility of structural materials with chloride molten salt. In this study, electrochemical methods were applied to investigate the corrosion kinetics and mechanisms of pure Ni, Fe, Cr, SS316, and A709 in thermally and chemically purified molten $MgCl_2-KCl-NaCl$ salt to explore the underlying corrosion mechanisms. It was found that the corrosion of metals and alloys in the salt was governed by the diffusion of corrosive impurities at temperatures of 600, 650, and 700 °C. The corrosion rates of each metal/alloy were determined using Tafel analysis under impurity diffusion-controlled conditions. The results showed that the corrosion resistance hierarchy for pure metals was Ni > Fe > Cr, while for alloys, SS316 demonstrated superior corrosion resistance compared to A709 within the tested temperature range and conditions.

1. Introduction

The escalating issue of energy consumption and its detrimental impact on greenhouse gas emissions represents a significant global challenge. Among sustainable energy sources, nuclear and solar energy are expected to play pivotal roles in future electricity generation. Next-generation concentrated solar power (CSP) plants and advanced nuclear power systems, such as molten salt reactors, are designed to achieve higher power cycle efficiencies by operating at temperatures exceeding 600 °C. Consequently, chloride molten salts are considered promising candidates for high-temperature applications due to their favorable thermophysical properties as heat transfer fluids and thermal energy storage media.[1] However, structural material degradation remains a critical challenge in the application of molten salts in both nuclear and solar power plants, primarily influenced by the chemistry of the molten salt and the properties of the containment vessel materials.[2–4]

For structural material corrosion studies, sample immersion tests in crucibles[5,6] and electrochemical corrosion measurement methods[7,8] are widely utilized. Electrochemical corrosion methods involve applying advanced electrochemical techniques to evaluate the rate and extent of corrosion processes occurring at the metal-molten salt interface.[9–11] Among these, the potentiodynamic (PD) scan is a commonly used technique,[12] providing critical data for material selection, molten salt chemistry optimization, and the development of corrosion

mitigation strategies.[13–16] Although PD is a powerful method to study corrosion mechanisms, significant methodological inconsistencies exist. These inconsistencies include performing partial fits to either the cathodic or anodic branch[17–19] or applying fits across both branches under ideal and non-ideal conditions.[20,21] The application of PD in molten salt system needs more investigation.

For structural material selection, it is known that nickel-based superalloys are particularly attractive due to their high corrosion resistance in molten salt applications,[16] therefore, most previous studies on corrosion in molten salt focused on Ni-based alloys. However, their extremely high cost poses a significant barrier to widespread implementation. In contrast, iron-based alloys, such as SS316, are considered primary candidates for construction materials in such environments.[22] Since 2013, Argonne National Laboratory in Illinois, USA (ANL), Idaho National Laboratory in Idaho, USA (INL), and Oak Ridge National Laboratory in Tennessee, USA (ORNL) have collaborated to evaluate Alloy 709 (A709), an austenitic stainless steel, as a material for nuclear power plants.[23] Research findings indicate that A709 exhibits exceptional strength, toughness, good fatigue resistance, and notable corrosion resistance in atmospheric conditions.[24,25] Therefore, the present study focuses on corrosion of SS316 and A709 in molten chloride salts for which experimental data are still scarce.

It has been recognized that corrosive impurities, such as H^+, OH^-, Ni^{2+}, are the primary contributors to corrosion[26,27] in molten salts. Therefore, previous studies on molten salt corrosion have largely focused on introducing corrosive impurities into the system to assess their effects.[28–30] The corrosion

Nuclear Engineering Program, Department of Mechanical Engineering, Virginia Tech, Blacksburg, VA 24061, USA. E-mail: zjinsuo5@vt.edu

mechanisms in purified molten salt with very low corrosive impurities are not well identified and the exploration of low-impurity-diffusion-controlled electrochemical corrosion in chloride salt systems remains limited.

In this study, we conducted electrochemical investigations on three pure metals (Ni, Cr, Fe) and two alloys (SS316 and Alloy 709) in chemically purified molten $MgCl_2$–NaCl–KCl salt (53.9–24.4–21.8 wt%, 44.7–25.8–29.4 mol%), referred to in this paper as Magnak. This composition was recommended by the National Renewable Energy Laboratory in Colorado, USA (NREL) in 2019 as a potential candidate for third-generation concentrated solar power plants.[31] This eutectic salt has a melting point of approximately 385 °C.[32] The study aims to investigate corrosion mechanisms in purified molten Magnak salt by conducting electrochemical tests on pure metals, including Ni, Fe, and Cr, as well as iron-based alloys such as SS316 and A709.[33,34] The experiments were performed at temperatures ranging from 600 °C to 700 °C. Furthermore, an analytical approach was developed for interpreting PD scan data in systems governed by corrosive impurity diffusion.

2. Experimental

2.1 Molten salt preparation

The individual chloride salts—$MgCl_2$, KCl, and NaCl—were purchased separately from Thermo Fisher Scientific with a stated purity of 99%. These salts were stored under ambient conditions prior to the experiments. It is important to note that chloride salts are highly hygroscopic, meaning they readily absorb moisture during shipping and storage. To minimize impurity levels, the salts were transferred into a glovebox and subjected to a thermal purification process in alumina crucibles at 200 °C for over 24 hours. During this process, moisture and oxygen levels within the glovebox were carefully monitored. It was observed that both moisture and oxygen levels initially increased but returned to normal levels as the purification progressed.

The heat-treated salts were weighed using a high-precision digital balance (MS 105DU, Mettler Toledo) and physically mixed in alumina crucibles (MSE Supplies). The mixture underwent a thermal purification process based on a previously established method,[35] in furnace (FB1315M, Thermo Scientific). This process involved heating the salt mixture to 500 °C at a ramp rate of 3 °C min^{-1} and allowing it to settle for at least 5 hours. Afterward, the mixture was carefully poured onto a pure nickel plate to rapidly cool and solidify the salt. It is important to note that during this process, insoluble particles settled at the bottom of the crucible.

A clean alumina crucible was used to melt the physically separated and thermally purified Magnak salt at 500 °C, into which 10 wt% magnesium metal (Mg) was added to the molten salt. The system was then heated at a controlled rate of 3 °C min^{-1} until it reached 800 °C, where it was held isothermally for 2 hours. Subsequently, the system was cooled to 550 °C, and the remaining magnesium metal was carefully separated from the salt using appropriate tools.

The chemically purified salt was then allowed to settle for an additional 8 hours at 550 °C to facilitate the precipitation of MgO formed during the purification process. Following this, the same quenching process described earlier was applied. The chemical purification of Magnak salt to remove MgOHCl has been extensively studied by Zhao and Vidal.[36] Their report indicated that thermal purification alone did not significantly reduce the MgOHCl content. However, the introduction of magnesium metal effectively decreased the MgOHCl content to 0.11 wt%. In this study, the purified salt was characterized by electrochemical experiments using Gamry workstation (Interface 1000), inductively coupled plasma mass spectrometry (ICP-MS) (Agilent 7800 Agilent 7800), and G6 LEONARDO O/H analyzer (Bruker).

2.2 Metal sample preparation

The materials investigated in this study include Ni (99%, Alfa Aesar by Thermo Fisher Scientific), Fe (99%), and Cr (99.95%, American Elements). For comparison, two alloys, SS316 and A709, were also studied. The chemical compositions of these alloys are provided in Table 1. All materials, except for A709, were in rod form. The A709 samples were cuboid-shaped, with dimensions of 3 mm in width and 1.5 mm in thickness. The immersion depths of all samples were measured after the experiments. Prior to testing, the surfaces of all samples were polished using SiC sandpaper with progressively finer grit sizes, ranging from 240 to 1200.

2.3 Electrochemical corrosion testing methods

A three-electrode electrochemical cell (Fig. 1) was employed as described in previous studies.[35,37] In this study, we modified a Mg^{2+}/Mg metal reference electrode (RE) based on our earlier work.[35] An image of the Mg^{2+}/Mg reference electrode is shown in Fig. 1. The Mg^{2+}/Mg reference electrode was integrated into an alumina tube with a 1 mm hole drilled at the bottom, allowing molten salt to flow into the tube and to contact with the Mg metal electrode. Experimental results confirmed the stability of the reference electrode throughout the duration of the experiments.

Electrochemical corrosion experiments were conducted at three temperatures, gradually increasing from 600 °C to 700 °C, within a glovebox filled with pure argon gas. The glovebox environment-maintained oxygen levels at 15 ppm and moisture levels at 2–3 ppm. The procedure began by ramp-heating a 30 g

Table 1 Chemical composition of SS316 and A709 in wt%

Elements	Cr	Ni	Fe	Mn	Mo	Si	Nb	Ti
A709	19.93	24.98	~52	0.91	1.51	0.44	0.2	0.04
SS316	18–20	11–14	59–67	1–2.5	2–3	0.3–0.65	—	—

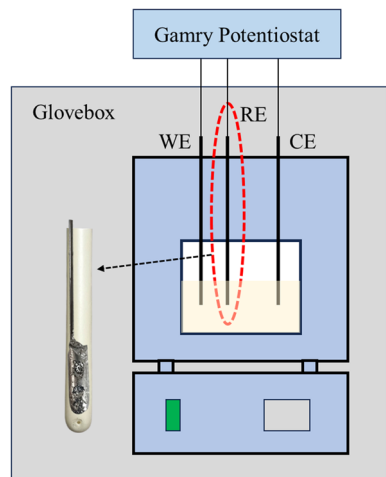| Elements	Cu	N	C	P	B	S
A709	—	0.148	0.066	0.014	0.0045	—
SS316	0.75	—	0.03	0.03	—	0.03

Paper

Fig. 1 Three-electrode electrochemical cell setup and pictures of Mg^{2+}/Mg reference electrode and alumina container. RE: Mg^{2+}/Mg, WE: tungsten or corrosion sample, CE: counter electrode, tungsten.

sub-batch of salt in an alumina crucible at a rate of 5 °C min^{-1} until reaching 600 °C. At this temperature, ICP-MS samples were collected, and cyclic voltammetry (CV) scans were performed using a tungsten working electrode (WE) before introducing the corrosion specimens. Once the corrosion specimens were inserted, open circuit potential (OCP) measurements were conducted for 1 hour. This was followed by a potentiodynamic (PD) scan in the positive direction at a rate of 2 mV s^{-1},[15] within a scan window of ± 0.25 V relative to the OCP. The selected scan

rate was designed to minimize the release of corrosion products into the molten salt. For tests on pure metals, one specimen was tested at each temperature. In contrast, when studying alloys, three separate specimens were tested at each temperature to ensure reproducibility.

3. Results and discussion

3.1 Salt impurity analysis

Fig. 2 shows the CV curves of each sub-batch of salt before immersing the test samples at 600 °C, using a scan rate of 100 mV s^{-1}. The prominent peaks observed at the left end correspond to the redox reaction of the Mg^{2+}/Mg couple, occurring near zero potential. The stability provided by the Mg^{2+}/Mg reference electrode ensures consistent potential measurements across different tests. The scanning potential range was fixed between -0.025 V and 2 V. Within this range, two weak impurity peaks were detected between 1 and 1.25 V *vs.*

Table 3 O/H concentration of Magnak salt at each stage

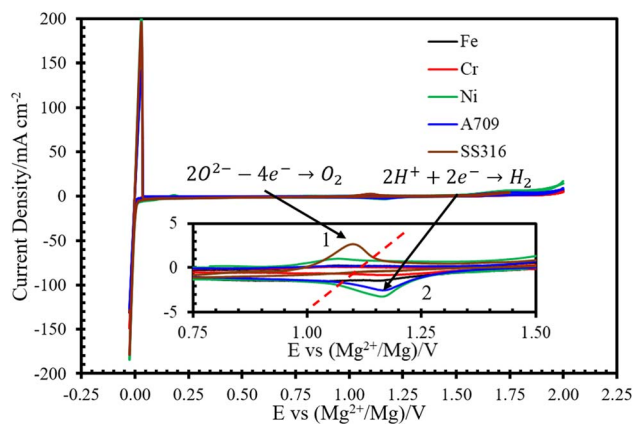|	O (wppm)		H (wppm)	
Salt	Average	St. dev	Average	St. dev
As received	7343	998	672	117
Thermally purified	183	22	228	25
Chemical purified	66	22	48	30

Fig. 2 Cyclic voltammetry scans of each sub-batch salt at 600 °C with scan rate at 100 mV s^{-1}, the WE is tungsten, the RE is Mg^{2+}/Mg, and CE was tungsten.
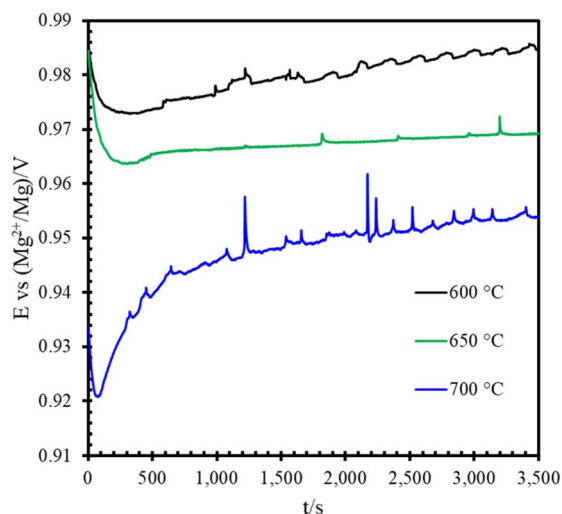

Fig. 3 One-hour OCP curve of pure Fe sample before conducting PD scan. WE: iron, RE: magnesium, CE: tungsten.

Table 2 ICP-MS result of the sub-batch salt before pure metal testing (unit: mole%)

	Na	Mg	K	Fe	Ni	Cr
Sub-batch_Fe	28.92	44.93	26.16	$<1.25 \times 10^{-6}$	$<1.17 \times 10^{-6}$	3.64×10^{-3}
Sub-batch_Ni	29.12	44.66	26.23	$<8.51 \times 10^{-7}$	$<7.95 \times 10^{-7}$	2.48×10^{-3}
Sub-batch_Cr	29.23	44.34	26.43	$<6.40 \times 10^{-7}$	$<5.97 \times 10^{-7}$	1.52×10^{-3}
Average	29.09	44.64	26.27	$<9.15 \times 10^{-7}$	$<8.54 \times 10^{-7}$	2.55×10^{-3}

Mg^{2+}/Mg. ICP results (Table 2) indicate that the major metallic impurities are below detectable levels, suggesting that the impurities are non-metallic in nature. The O/H concentrations in the salt at each stage were measured, and the results presented in Table 3. These samples, collected from different purification batches but subjected to the same procedure, confirm that chemical purification effectively reduces oxygen and hydrogen content. This indicates that both metallic and non-metallic (O and H) impurities were minimal in the salt. Evidently based on the CV scan results in Fig. 2, the oxidation peaks' potential (1) was more negative than that of the reduction peaks (2), indicating distinct reaction origins for these peaks. According to Kanzaki and Takahashi's[38] calculations, peak (1) corresponds to the reaction of $2O^{2-} - 4e^- \rightarrow O_2$,

possessing a standard potential of -1.173 V $vs.$ Cl_2/Cl^-. On the other hand, peak (2) corresponds to the reaction of $2H^+ + 2e^- \rightarrow H_2$, with a standard potential of -1.016 V $vs.$ Cl_2/Cl^-. Both O_2 and H_2 are released from the system, resulting in the absence of discernible reverse peaks.

3.2 Electrochemical corrosion test of pure metals

The CV scan and ICP-MS results confirmed the presence of minor impurities in the chemically purified Magnak salt. Before performing the PD scan, a one-hour OCP measurement was conducted to monitor the system's equilibrium.

Fig. 3 shows the OCP results for Fe at various temperatures. Generally, the OCP of the metal specimens increased with
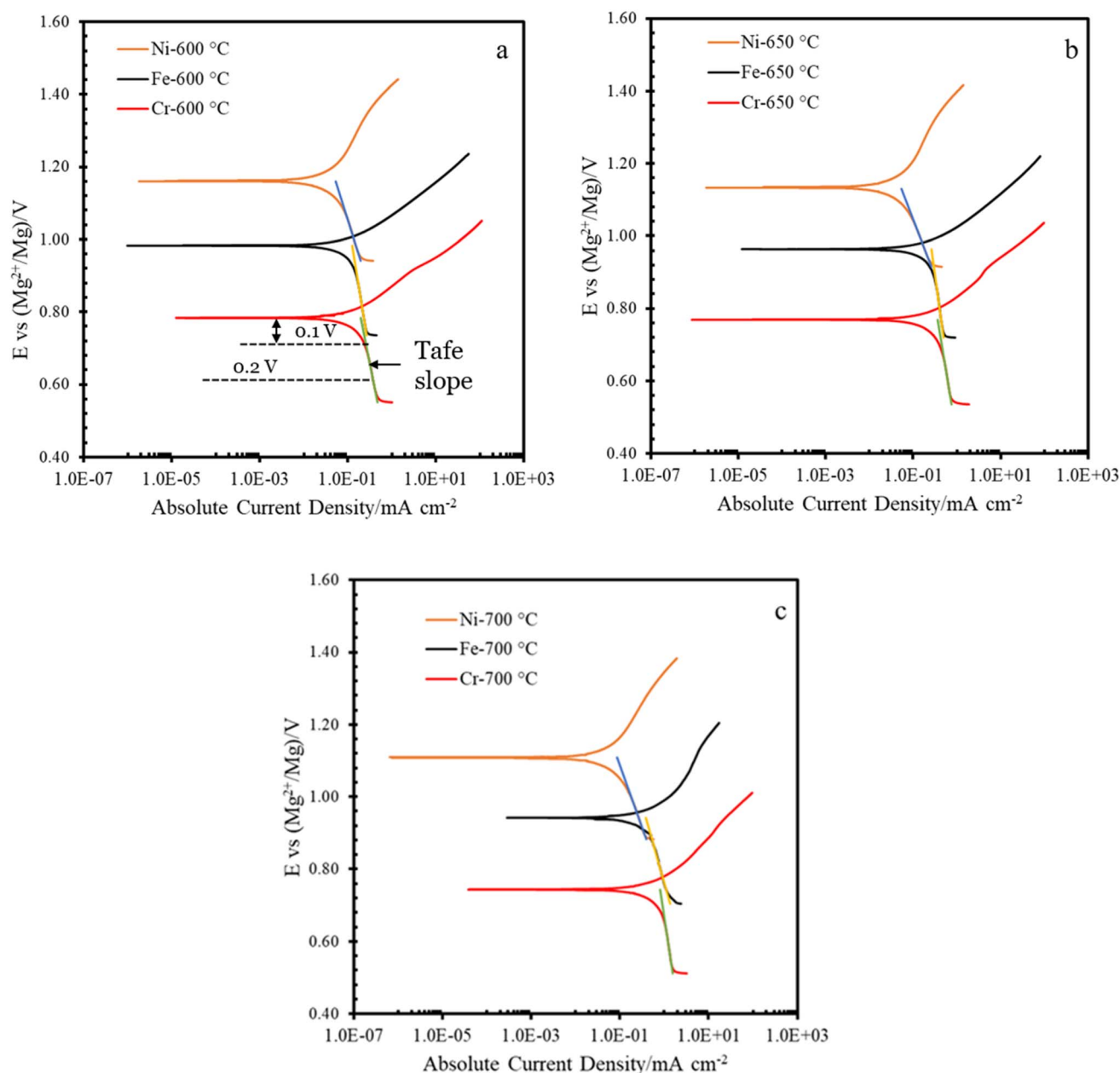

Fig. 4 PD scan of pure metals in molten Magnak at (a) 600 °C, (b) 650 °C, (c) 700 °C.

immersion time, reflecting continuous corrosion during the measurement process, as depicted in the figure.

Following the OCP measurement, a PD scan was carried out over a range of ±0.25 V relative to the OCP, with a scan rate of 2 mV s^{-1}. Fig. 4(a)–(c) present the PD curves for the pure metals at different temperatures. The PD scan was initiated from the negative potential direction and swept toward the positive potential relative to the OCP. As noted previously, corrosion during the one-hour OCP measurement introduced corrosion products into the salt. This explains the initially higher PD current, which rapidly dropped within the first 10–15 mV of the sweep. Once the corrosion products near the working electrode (WE) surface were consumed, the cathodic current became dominated by the reduction of impurities. Fig. 4(a) and (b) show that the cathodic current density slopes for Fe and Cr were very similar within the scan range of approximately −0.2 V to −0.1 V, whereas Ni exhibited a distinctly different behavior. The similarity between Fe and Cr was attributed to the fact that the cathodic current was limited by the diffusion of impurities in the salt when the overpotential was sufficiently negative. At 600 °C, the PD curves revealed that Fe and Cr were governed by impurity diffusion control, whereas Ni fell into the impurity activation control region. As the temperature increased, the diffusion rate of impurities also rose, leading to a broader activation zone. Consequently, at 700 °C, the slope of the Fe corrosion curve approached that of Ni.

The corrosion potentials of the materials were determined using both the OCP method and the PD scan method at various temperatures, as listed in Table 4. In this study, the corrosion potentials obtained from the OCP method (E_{corr}^{OCP}) were consistently more positive than those obtained from the PD scans (E_{corr}^{PD}) as shown in the table. The phenomenon was described by de Assis et al.[39] as being attributed to the large initial reduction potential that disrupts the passive layer, resulting in a switch to a more negative potential in aqueous solutions. However, this explanation may not apply to molten salt environments due to the instability of the passive layer in these systems. Furthermore, Zhang et al.[12] highlighted that de Assis et al.'s theory fails

to explain why E_{corr}^{PD} shifts further to negative potentials as the PD scan rate increases in aqueous solutions.

Brad and Faulkner[40] examined the role of double-layer capacitance in potential sweep experiments. They observed that a charging current density ($i_{charging}$) proportional to the scan rate and interface capacitance is always present. In a PD scan, the E_{corr}^{PD} of the polarization curve occurs when the total current density (i) equals zero. The total current i^{PD} is given by:

$$i^{PD} = i_{charging} + i_a + i_c \quad (1)$$

In eqn (1), i_c and i_a refer to the cathodic current density and anodic current density. For OCP measurements, there is no charge current involved, resulting in a total current of zero when $i_a = -i_c$. However, during a PD scan, the positive charge stored in the interface capacitor continues to increase, indicating that electrons are being driven away from the interface by the external power source. Consequently, the charging current flows in the same direction as the anodic current during a positive scan. As a result, a lower E_{corr}^{PD} is required to achieve a total current density of zero compared to E_{corr}^{OCP}. It is worth noting that a higher scan rate results in a larger charging current density and a greater potential shift. In our current experiments, the results presented in Table 4 indicate that, except for Fe, all other samples exhibited a potential shift ranging from 17 to 30 mV in the negative direction. This discrepancy is shown as an error in Fig. 5. In Fig. 5, the potentials were converted from the Mg^{2+}/Mg reference electrode to the Cl$_2$ reference electrode using the redox potential correlation reported by Zhang et al.[35]

Once the potential difference between E_{corr}^{OCP} and E_{corr}^{PD} is known, the corrosion current density, typically determined using the intersection of E_{corr}^{PD} with the cathodic current density

Table 4 Corrosion potentials (vs. Mg^{2+}/Mg) obtained from OCP and PD tests at varying temperatures

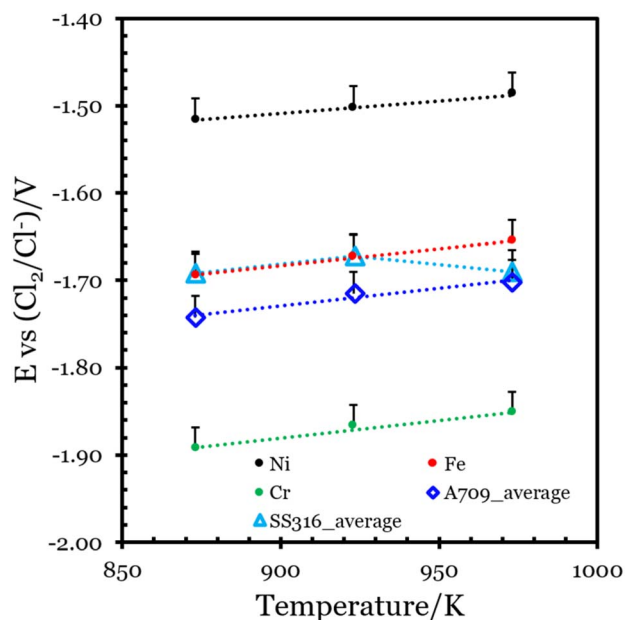| Temp. (°C)	Samples	E_{corr}^{OCP} (V)	E_{corr}^{PD} (V)	$E_{corr}^{OCP} - E_{corr}^{PD}$ (V)
600	Fe	0.985	0.983	0.002
	Ni	1.190	1.161	0.029
	Cr	0.801	0.784	0.017
	A709	0.960 ± 0.004	0.935 ± 0.005	0.025
	SS316	1.011 ± 0.005	0.985 ± 0.004	0.026
650	Fe	0.969	0.964	0.005
	Ni	1.170	1.134	0.036
	Cr	0.786	0.769	0.017
	A709	0.949 ± 0.001	0.922 ± 0.004	0.027
	SS316	0.985 ± 0.003	0.965 ± 0.002	0.020
700	Fe	0.954	0.941	0.013
	Ni	1.130	1.109	0.021
	Cr	0.761	0.744	0.017
	A709	0.918 ± 0.008	0.895 ± 0.005	0.023
	SS316	0.928 ± 0.005	0.906 ± 0.005	0.022

Fig. 5 Corrosion potential from potentiodynamic scan of pure metals and alloys.
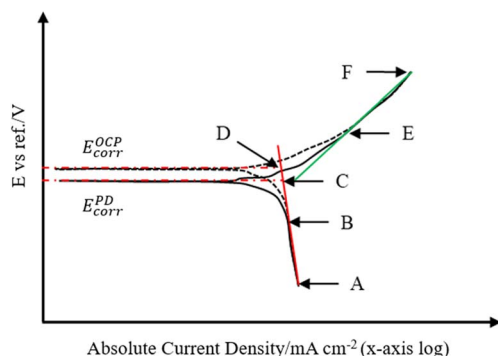
Fig. 6 Theoretical PD curves for illustration of the correlation between the OCP corrosion current density and PD corrosion current density under cathodic diffusion-controlled condition.

when corrosion is controlled by the cathodic reaction becomes less accurate. Fig. 6 illustrates the correlation between the OCP corrosion current density and the PD corrosion current density. The charge current density influences the PD current density. Since the i_{charge} in the same direction as i_a, it reduces E_{corr}^{OCP} to E_{corr}^{PD} within the potential range B to C (see Fig. 6). However, within the potential range of A to B, when i_c is significantly higher, the influence of i_a and i_{charge} is minimal. Extending the cathodic fitting line (solid red) in the A to B range allows determination of its intersection with E_{corr}^{OCP}, which, through eqn (2), yields the corrosion current density at E_{corr}^{OCP}. Importantly, regardless of whether the cathodic PD curve lies within the impurities' activation zone or diffusion zone, at E_{corr}^{OCP}, the cathodic current density remains lower than the anodic current density. This observation signifies that the cathodic current density corresponds to the i_{corr}^{OCP}. Consequently, the corresponding corrosion current density at E_{corr}^{OCP} is calculated and detailed presented in Table 5.

$$\log(|i^{OCP}|) = \log(|i^{PD}|) - \frac{E_{corr}^{OCP} - E_{corr}^{PD}}{\beta_c} \quad (2)$$

Upon analyzing the results, the disparity between the corrosion current densities determined using the corrosion potential from the PD and OCP methods for pure Fe and Cr is approximately 10%. However, for Ni, the corrosion current density exhibits a 20% difference between the two methods. This discrepancy arises due to Ni's inherently low current density at both the passivation potential (PD) and OCP. Consequently, even a slight variation in the current density results in a substantial change in the calculated ratio.

3.3 Electrochemical corrosion test of SS316 and A709

For alloys, the polarization curves obtained through PD exhibit significant differences compared to those of pure metals. Fig. 7(a) shows that the PD curves for the alloys display a wide noise band, with SS316 exhibiting a noise band of approximately 30 mV and A709 around 20 mV. To enhance data visualization, a smoothing filter was applied to the current data using the Gamry Echem Analyst software. Specifically, a Savitzky–Golay filter of the fourth order with 16 points was utilized. Fig. 7(b) illustrates the three smoothed curves of A709 obtained at 600 °C. These curves correspond to three individual A709 samples from the same sub-batch of salt, denoted as S1, S2, and S3. The obtained E_{corr}^{OCP} and E_{corr}^{PD} values from the smoothed curves of the alloys at different temperatures were compiled in Table 4. The standard deviations of the corrosion potentials were less than 8 mV, indicating high reliability and repeatability of the results. The corrosion potentials determined using the PD method for the alloys were also plotted in Fig. 5.

Additionally, for alloys, the Nernst potential of the majority element shifts positively compared to the Nernst potential of the corresponding pure metal because the activity coefficient of the element in the alloy. Therefore, even though A709 and SS316 contain Cr, their corrosion potential is significantly higher than that of pure chromium metal. As shown in Fig. 5, at 600 °C and 650 °C, SS316 exhibits a similar corrosion potential as pure Fe. However, at 700 °C, the corrosion potential of SS316 decreases

Table 5 Summary of cathodic slope and corrosion current density

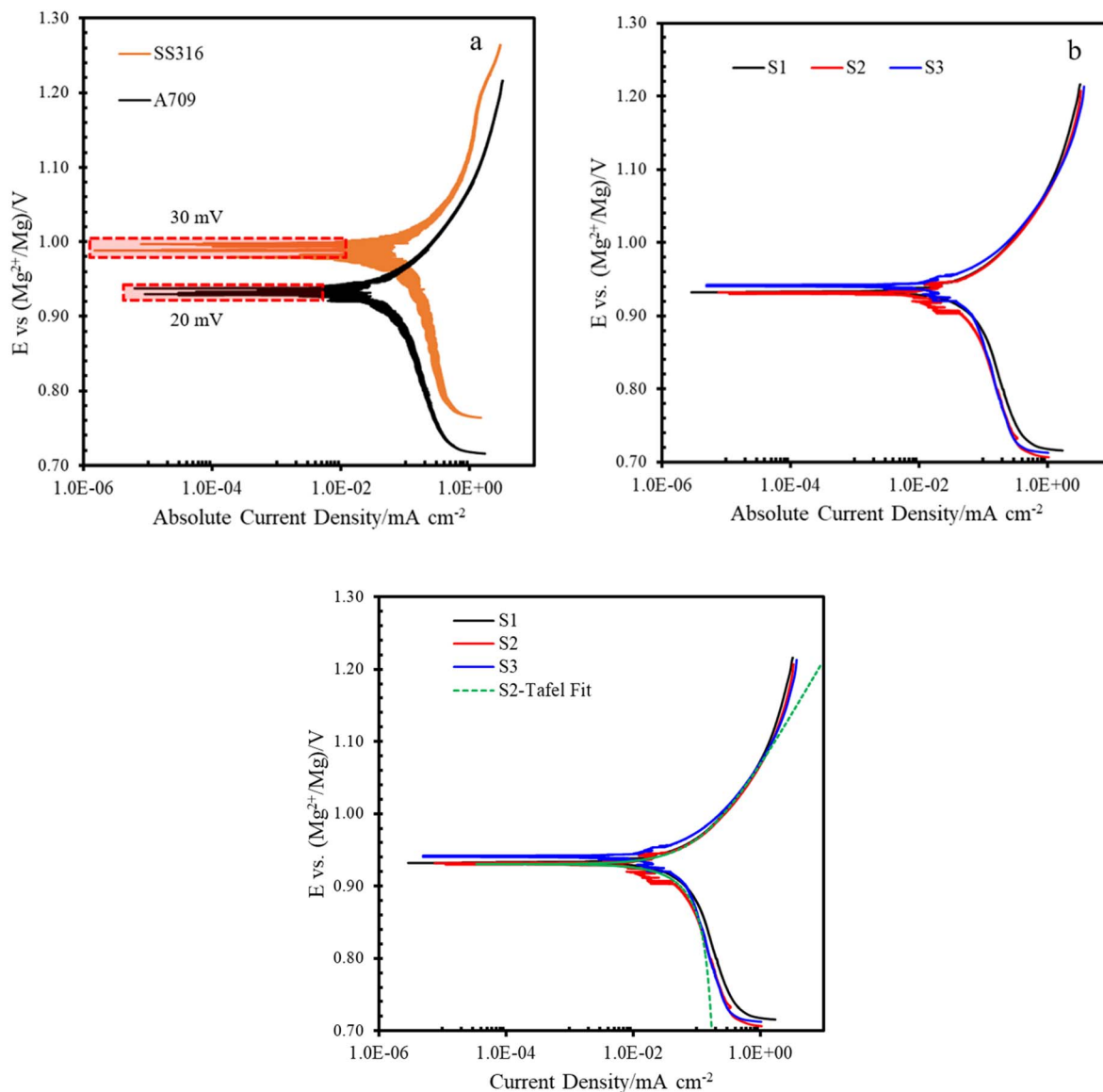| Temp. (°C)	Samples	Slope β_c (V per decade)	i_{corr}^{PD} (mA cm^{-2})	i_{corr}^{PD} (mA cm^{-2}) Tafel fitting	i_{corr}^{OCP} (mA cm^{-2})	$i_{corr}^{PD} - i_{corr}^{OCP}$ (mA cm^{-2})	$\frac{i_{corr}^{PD} - i_{corr}^{OCP}}{i_{corr}^{OCP}}$ (%)
600	Fe	0.7505	0.1256		0.1248	0.0008	0.6155
	Ni	0.3853	0.0528		0.0444	0.0084	18.9230
	Cr	0.6104	0.1965		0.1842	0.0123	6.7034
	SS316	0.4347	0.1240	0.4511	0.1147	0.0093	8.0935
	A709	0.2846	0.1484	0.1580	0.1371	0.0113	8.2041
650	Fe	0.8766	0.2616		0.2581	0.0034	1.3220
	Ni	0.3130	0.0525		0.0403	0.0122	30.3215
	Cr	0.7327	0.3626		0.3442	0.0184	5.3552
	SS316	0.5533	0.2605	0.8437	0.2426	0.0179	7.3779
	A709	0.3074	0.2924	0.2677	0.2772	0.0152	5.4862
700	Fe	0.4823	0.4161		0.3907	0.0254	6.5047
	Ni	0.3439	0.0861		0.0748	0.0113	15.0971
	Cr	0.8193	0.8079		0.7696	0.0383	4.9822
	SS316	0.3598	0.4942	0.4470	0.4433	0.0508	11.4642
	A709	0.3746	0.5197	0.4302	0.4677	0.0520	11.1276

Fig. 7 Potentiodynamic scan of alloys. (a) Original data of the first sample of SS316 and A709 at 600 °C. (b) Smoothed PD curves of three A709 samples at 600 °C.

to a value lower than Fe. The corrosion potential of A709 remains consistently lower than that of pure iron, with a difference of approximately 50 mV.

Considering that the E_{corr}^{OCP} of SS316 and A709 are close to that of pure Fe, it suggests that the potential scan region in the PD falls within the impurity diffusion control region because of the same impurity level of salts used for corrosion tests of pure Fe and alloys. For comparisons, the PD curves of A709, SS316, and pure metals at different temperatures were shown in Fig. 8. A709 exhibits a lower cathodic current compared to pure Fe at the same electrode potential, as the its corrosion potential is lower than that of pure Fe based on the polarization dynamic scan as shown in Fig. 8. This indicates that certain alloying components are readily oxidized in the alloy. The resulting oxidation current compensates for the impurity reduction current. The metal elements in SS316 have a relative higher Nernst potential result in a less oxidation current compared to

pure Fe. At 700 °C, the Nernst potential of the elements reduced sufficiently but still comparable higher than that in A709. It was observed that SS316 exhibits a higher cathodic current density, whereas A709's cathodic current density is lower when compared to the baseline Fe curve.

Although the concentration of corrosion products at the beginning of the electrochemical corrosion tests is too low to significantly influence the cathodic current, the dissolution of Cr below the corrosion potential of the alloy can still affect the cathodic current. Therefore, to accurately determine the corrosion current of the alloys under conditions where impurity diffusion controls the process, it is necessary to use auxiliary impurity data derived from pure Fe rather than fitting the PD curves of the alloys. The calculation is detailed in eqn (3).

$$\log\left(\left|i^{\text{alloy}}\right|\right) = \log\left(\left|i_{\text{Fe}}^{\text{PD}}\right|\right) - \frac{E_{\text{corr-alloy}}^{\text{i}} - E_{\text{corr-Fe}}^{\text{PD}}}{\beta_{\text{c-Fe}}} \quad (3)$$
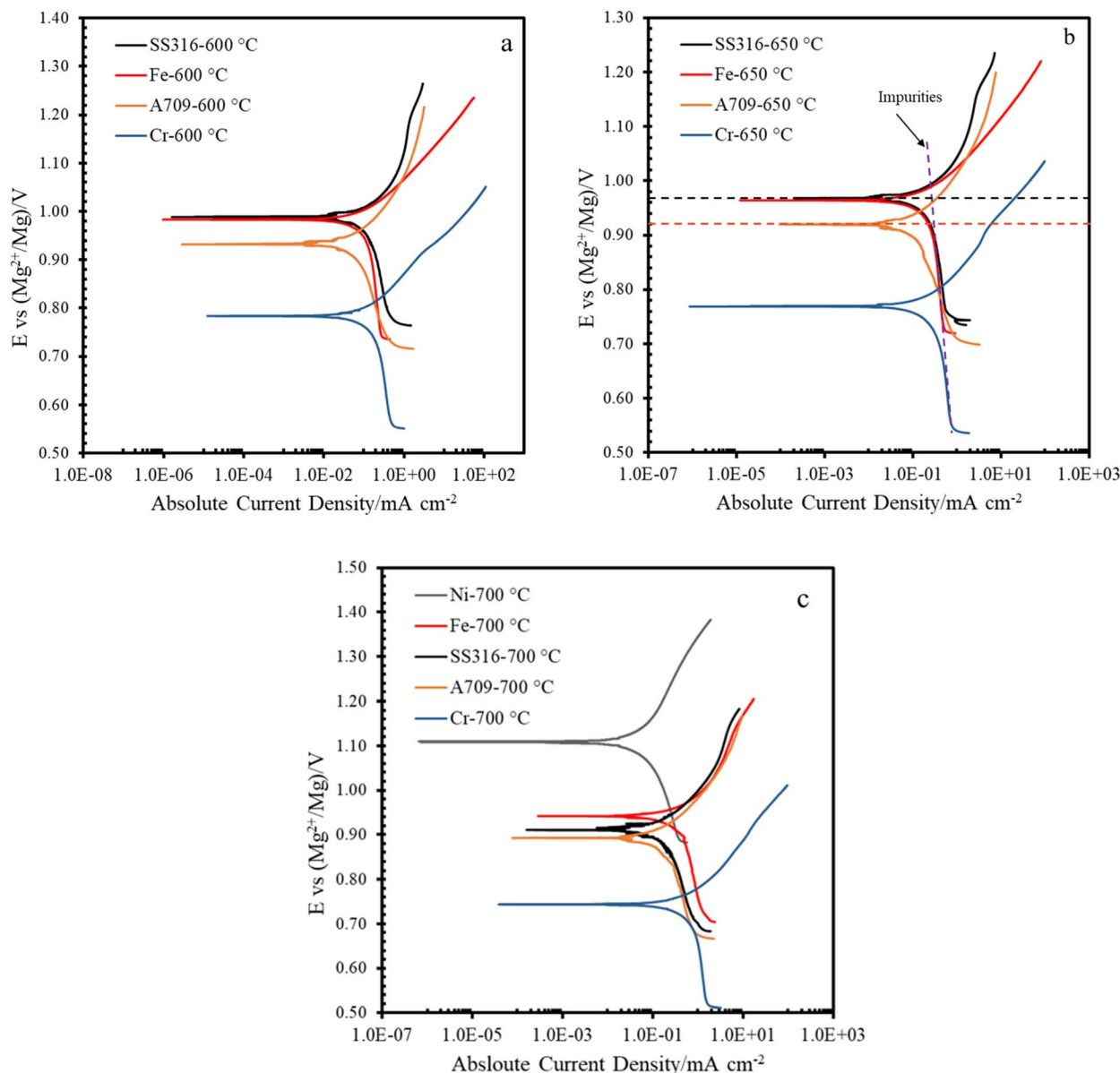
Fig. 8 The smoothed potentiodynamic scan curves of first sample of A709 and SS316 and pure metal PD curves at various temperatures. In (b), the purple line represents the cathodic PD curve and Nernst potential of impurities, the green and blue lines represent the anodic PD curves and Nernst potentials of A709 and SS316, respectively.

where $E_{corr-alloy}^{i}$ represents either $E_{corr-alloy}^{OCP}$ and $E_{corr-alloy}^{PD}$. The calculated corrosion current by eqn (3) as well as by directly Tafel fitting of the PD curves were given in Table 5. For the cases of 600 and 650 °C, the corrosion current density derived from eqn (3) is lower than that determined from the dissolution current density. This suggests that the corrosion process is governed by impurity diffusion. While for the case of 700 °C, the corrosion currents obtained by Tafel fitting for both of A709 and SS316 are comparable with the currents obtained by eqn (3). Despite the presence of wide noise in the PD curve, which increases the error associated with the E_{corr}^{PD}, the use of the corrosion correction eqn (2) by using $E_{corr-alloy}^{OCP}$ helps mitigate the errors introduced by data smoothing techniques.

4. Conclusion

The observed corrosion mechanism of pure metals (Fe, Cr, Ni) in low-impurity Magnak salt was found to be diffusion-controlled and dominated by cathodic reactions. By assuming that corrosion is governed by the corrosive impurity diffusion-limited current density, the corrosion kinetics of pure metals and two alloys (A709 and SS316) were studied. The results indicate that at 600 °C and 650 °C, the corrosion potential of SS316 is comparable to that of pure Fe. The corrosion current densities based on the corrosion potential measured by OCP for SS316 were 0.1147 mA cm^{-2} at 600 °C, 0.2426 mA cm^{-2} at 650 °C, and 0.4433 mA cm^{-2} at 700 °C. For A709, the

corrosion current densities were slightly higher, recorded at 0.1371 mA cm^{-2} at 600 °C, 0.2772 mA cm^{-2} at 650 °C, and 0.4677 mA cm^{-2} at 700 °C, showing a clear increase with temperature. In summary, the methodology employed for the PD electrochemical corrosion tests in this study effectively overcomes the limitations of the Tafel method, particularly under conditions governed by cathodic diffusion limitations. Data are available upon request from the authors.

Data availability

All data is available within the article.

Author contributions

Mingyang Zhang: conceptualization, data curation, methodology, formal analysis, investigation, writing – original draft. Amanda Leong: project administration, writing – review & editing. Siheng Ren: investigation. Jinsuo Zhang: conceptualization, validation, supervision, funding acquisition, writing – review & editing.

Conflicts of interest

The authors declare that they have no known competing financial interests or personal relationships that could have appeared to influence the work reported in this paper.

Acknowledgements

References

1 M. Mehos, C. Turchi, J. Vidal, M. Wagner, Z. Ma, C. Ho, et al., *Concentrating Solar Power Gen3 Demonstration Roadmap*, National Renewable Energy Lab.(NREL), Golden, CO (United States), 2017.

2 S. Guo, J. Zhang, W. Wu and W. Zhou, Corrosion in the molten fluoride and chloride salts and materials development for nuclear applications, *Prog. Mater Sci.*, 2018, **97**, 448–487.

3 J. Zhang, C. W. Forsberg, M. F. Simpson, S. Guo, S. T. Lam, R. O. Scarlat, et al., Redox potential control in molten salt systems for corrosion mitigation, *Corros. Sci.*, 2018, **144**, 44–53.

4 P. M. Singh, K. J. Chan, C. S. Deo, V. Deodeshmukh, J. R. Keiser, W. Ren, et al., Phenomena Identification and Ranking Table (PIRT) study for metallic structural materials for advanced High-Temperature reactor, *Ann. Nucl. Energy*, 2019, **123**, 222–229.

5 K. Patel, V. Hasannaeimi, M. Sadeghilaridjani, S. Muskeri, C. Mahajan and S. Mukherjee, Molten Salt Corrosion Behavior of Dual-Phase High Entropy Alloy for Concentrating Solar Power Systems, *Entropy*, 2023, **25**(2), 296.

6 C. V. Bhave, G. Zheng, K. Sridharan, D. Schwen and M. R. Tonks, An electrochemical mesoscale tool for modeling the corrosion of structural alloys by molten salt, *J. Nucl. Mater.*, 2023, **574**, 154147.

7 R. I. Holland, Use of potentiodynamic polarization technique for corrosion testing of dental alloys, *Eur. J. Oral Sci.*, 1991, **99**(1), 75–85.

8 S. Esmailzadeh, M. Aliofkhazraei and H. Sarlak, Interpretation of cyclic potentiodynamic polarization test results for study of corrosion behavior of metals: a review, *Prot. Met. Phys. Chem. Surf.*, 2018, **54**, 976–989.

9 Y. Yi, P. Cho, A. Al Zaabi, Y. Addad and C. Jang, Potentiodynamic polarization behaviour of AISI type 316 stainless steel in NaCl solution, *Corros. Sci.*, 2013, **74**, 92–97.

10 R. Holland, Corrosion testing by potentiodynamic polarization in various electrolytes, *Dent. Mater.*, 1992, **8**(4), 241–245.

11 S. Munir, M. H. Pelletier and W. R. Walsh, Potentiodynamic corrosion testing, *J. Visualized Exp.*, 2016, (115), e54351.

12 X. Zhang, Z. H. Jiang, Z. P. Yao, Y. Song and Z. D. Wu, Effects of scan rate on the potentiodynamic polarization curve obtained to determine the Tafel slopes and corrosion current density, *Corros. Sci.*, 2009, **51**(3), 581–587.

13 J. C. Gomez-Vidal and R. Tirawat, Corrosion of alloys in a chloride molten salt (NaCl-LiCl) for solar thermal technologies, *Sol. Energy Mater. Sol. Cells*, 2016, **157**, 234–244.

14 W. H. Doniger, A. Couet and K. Sridharan, Potentiodynamic polarization of pure metals and alloys in molten LiF-NaF-KF (FLiNaK) using the K/K+ dynamic reference electrode, *J. Electrochem. Soc.*, 2022, **169**(7), 071502.

15 T. Ghaznavi, S. Y. Persaud and R. C. Newman, Electrochemical corrosion studies in molten chloride salts, *J. Electrochem. Soc.*, 2022, **169**(6), 061502.

16 K. Vignarooban, P. Pugazhendhi, C. Tucker, D. Gervasio and A. M. Kannan, Corrosion resistance of Hastelloys in molten metal-chloride heat-transfer fluids for concentrating solar power applications, *Sol. Energy*, 2014, **103**, 62–69.

17 M.-C. Zhao, P. Schmutz, S. Brunner, M. Liu, G.-L. Song and A. Atrens, An exploratory study of the corrosion of Mg alloys during interrupted salt spray testing, *Corros. Sci.*, 2009, **51**(6), 1277–1292.

18 Z. Shi, M. Liu and A. Atrens, Measurement of the corrosion rate of magnesium alloys using Tafel extrapolation, *Corros. Sci.*, 2010, **52**(2), 579–588.

19 M. Stratmann and G. S. Frankel, *Corrosion and oxide films*, Wiley-VCH, Weinheim, 2003.

20 L. Xu and Y. Cheng, Development of a finite element model for simulation and prediction of mechanoelectrochemical effect of pipeline corrosion, *Corros. Sci.*, 2013, **73**, 150–160.

21 J. Ge and O. Isgor, Effects of Tafel slope, exchange current density and electrode potential on the corrosion of steel in concrete, *Mater. Corros.*, 2007, **58**(8), 573–582.

22 S. Chang, Y. Jia, X. Du and S. Guo, Corrosion behavior of commercial alloys in LiCl–KCl molten salt containing EuCl3, *Front. Mater.*, 2022, **9**, 958296.

23 K. Natesan, X. Zhang, T.-L. Sham and H. Wang, *Report on the Completion of the Procurement of the First Heat of Alloy 709*, Argonne National Lab.(ANL), Argonne, IL (United States); 2017.

24 A. Lall, P. Bowen and A. Rabiei, A study on the creep behavior of alloy 709 using in-situ scanning electron microscopy, *Mater. Charact.*, 2022, **183**, 111587.

25 Y. Zhao, R. Schoell, C. Zheng, M. N. Cinbiz, M. Frost, K. An, *et al.*, Creep properties of advanced austenitic steel 709 determined through short experiments under in-situ neutron diffraction followed by TEM characterization, *Mater. Charact.*, 2021, **182**, 111519.

26 W. H. Doniger, C. Falconer, M. Elbakhshwan, K. Britsch, A. Couet and K. Sridharan, Investigation of impurity driven corrosion behavior in molten 2LiF-BeF2 salt, *Corros. Sci.*, 2020, **174**, 108823.

27 B. D'Souza, W. Zhuo, Q. Yang, A. Leong and J. Zhang, Impurity driven corrosion behavior of HAYNES® 230® alloy in molten chloride Salt, *Corros. Sci.*, 2021, **187**, 109483.

28 Y. L. Wang, Q. Wang, H. J. Liu and C. L. Zeng, Effects of the oxidants H2O and CrF3 on the corrosion of pure metals in molten (Li, Na, K) F, *Corros. Sci.*, 2016, **103**, 268–282.

29 V. Pavlik, M. Kontrik and M. Boča, Corrosion behavior of Incoloy 800H/HT in the fluoride molten salt FLiNaK+ MF x (MF x= CrF 3, FeF 2, FeF 3 and NiF 2), *New J. Chem.*, 2015, **39**(12), 9841–9847.

30 M. Zhu, S. Zeng, H. Zhang, J. Li and B. Cao, Electrochemical study on the corrosion behaviors of 316 SS in HITEC molten salt at different temperatures, *Sol. Energy Mater. Sol. Cells*, 2018, **186**, 200–207.

31 Molten chloride technology pathway to meet the US DOE sunshot initiative with Gen3 CSP, *AIP Conference Proceedings*, ed. Vidal J. C. and Klammer N., AIP Publishing, 2019.

32 P. Leung, S. C. Heck, T. Amietszajew, M. R. Mohamed, M. B. Conde, R. J. Dashwood, *et al.*, Performance and polarization studies of the magnesium–antimony liquid metal battery with the use of in-situ reference electrode, *RSC Adv.*, 2015, **5**(101), 83096–83105.

33 H. Kim, J. G. Gigax, J. Fan, F. A. Garner, T.-L. Sham and L. Shao, Swelling resistance of advanced austenitic alloy A709 and its comparison with 316 stainless steel at high damage levels, *J. Nucl. Mater.*, 2019, **527**, 151818.

34 J. Brnic, M. Canadija, G. Turkalj and D. Lanc, Structural steel ASTM A709—behavior at uniaxial tests conducted at lowered and elevated temperatures, short-time creep response, and fracture toughness calculation, *J. Eng. Mech.*, 2010, **136**(9), 1083–1089.

35 M. Zhang, J. Ge, T. Yin and J. Zhang, Redox potential measurements of Cr (II)/Cr Ni (II)/Ni and Mg (II)/Mg in molten MgCl2–KCl–NaCl mixture, *J. Electrochem. Soc.*, 2020, **167**(11), 116505.

36 Y. Zhao and J. Vidal, Potential scalability of a cost-effective purification method for MgCl2-Containing salts for next-generation concentrating solar power technologies, *Sol. Energy Mater. Sol. Cells*, 2020, **215**, 110663.

37 M. Zhang, J. Ge, J. Zhang and L. E. Liu, Redox potential measurement of AgCl in molten LiCl-KCl salt using chronopotentiometry and potentiodynamic scan techniques, *Electrochem. Commun.*, 2019, **105**, 106498.

38 Y. Kanzaki and M. Takahashi, The hydrogen electrode in fused lithium chloride-potassium chloride eutectic containing hydrogen ion, *J. Electroanal. Chem. Interfacial Electrochem.*, 1975, **58**(2), 349–356.

39 S. L. de Assis, S. Wolynec and I. Costa, Corrosion characterization of titanium alloys by electrochemical techniques, *Electrochim. Acta*, 2006, **51**(8–9), 1815–1819.

40 A. J. Bard and L. R. Faulkner, Fundamentals and applications, *Electrochem. Methods*, 2001, **2**(482), 580–632.